STUDY OF AN EDGE-BASED FINITE VOLUME SCHEME AT WING TRAILING EDGE AND THE INFLUENCE ON THE OVERALL ACCURACY

Lars Tysell
FOI, Swedish Defence Research Agency, SE-172 90 Stockholm, Sweden

Keywords: *Inviscid computations, Grid generation, Accuracy, Wing trailing edge*

Abstract

Inviscid flow computation have been done using a node-centered edge-based finite volume flow solver. The accuracy have been studied by computations on a series of grids around a set of airfoil type geometries in 2D and a wing section in 3D. It is shown that the local error introduced by the sharp trailing edge for an airfoil or a wing causes a small global error. The error is larger in 2D than in 3D. The error may be negligible for the cases studied here, but it may also be larger for other cases.

1 Background

Due to the increase in computer capacity the last decades it has become possible to do flow computations on more complex configurations with an ever increasing number of grid points. To compute viscous flow on grids with more than 10 Mpoints is now a daily routine. For some special studies grids with approximately 30-50 Mpoints are being used. For grids with this resolution on a simple wing/fuselage configuration it should be possible to do a series of computations on grids of different resolutions and extrapolate the results to infinite grid resolution. This has been done in the AIAA Drag Prediction Work Shop series [2], [4], [5] and [11]. Surprisingly these studies have shown that many solvers do not show the predicted asymptotic behaviour, and there is a big discrepancy between different solvers. Even the same solver may show different results for slightly different type of grids, suggesting the solutions are not grid converged. The aim of the AIAA Drag Prediction Work Shops series has been to study how well the current computational fluid dynamics tools can predict the drag. To do this within a few drag counts the computations must be very accurate.

2 Introduction

The order of accuracy has previously been studied for an edge-based finite volume flow solver. In [6] the accuracy questions were investigated for a number of model problems related to the Euler and Navier-Stokes equations for a node-centered edge-based finite volume method. This scheme should be second order accurate for very regular unstructured grids, but it is shown that for non-smooth grids the order of accuracy is lower. For two-dimensional hybrid grids with a non-smooth structured region or a non-smooth interface between the structured region and the unstructured region the order of accuracy may be much lower.

In [10] the accuracy of the Euler equation has been studied. There it has been shown that the accuracy for real life configurations is lower than second order, especially for two-dimensional configurations. Computations

of inviscid flow around a simple airfoil show the expected second order convergence on medium resolution grids, but on very fine grids the convergence was lower. The convergence of the drag decreased with increasing angle of attack, and the lift did not converge on very fine resolution grids, having an error of about 0.3% at 4.0 degrees angles of attack.

It is important to understand why we have this unexpected behaviour, otherwise we can not trust the results for more complex three-dimensional cases either. In this paper we will study the results of these test cases in more detail. We study some simple inviscid cases, since for these conditions we know what the solution (drag) should be.

3 Studied Configurations

Four two-dimensional configurations and one three-dimensional configuration have been studied. All configurations are located inside a box of $x \times y = 100.0 \times 50.0$ m, where the first number refers to the length of the box in the streamwise direction. For the three-dimensional case the dimension in the (spanwise) z-direction is 5.0 m. The studied configurations are varies kind of airfoils at $M_\infty = 0.3$ with a chord of 1.0 m. The top and bottom of the box are solid walls. The two-dimensional configurations studied are:

- A NACA 0012 airfoil placed in the middle of the box, see Figures 1-2. This configuration is called the 2D NACA 0012 configuration.
- The NACA 0012 airfoil divided into upper and lower parts, where the lower part is placed at the top of the box and the upper part at the bottom of the box, see Figures 3-4. This configuration is called the 2D double NACA 0012 configuration.
- The same as the previous one but where the trailing edge is modified in order to have a smooth transition to the box, see Figure 5. This configuration is called the 2D double smooth TE configuration.
- The same as the previous one but where also the leading edge is modified in order to have a smooth transition to the box, see Figure 6. This configuration is called the 2D double smooth LTE configuration.

The three-dimensional configuration studied is:

- A NACA 0012 wing section placed in the middle of the box. This configuration is called the 3D NACA 0012 configuration. This is the same configuration as the 2D NACA 0012 configuration, but with a spanwise extension, see Figure 7.

4 Grid Generation

An inhouse developed grid generation system called TRITET [7], [8] and [9], has been used for the grid generation. This grid generation system can be used for the generation of two-dimensional as well as three-dimensional unstructured/hybrid grids around complex geometries. The grid generator is based on the Advancing front algorithm. Tetrahedra of variable size, as well as directionally stretched tetrahedra can be generated by specification of a proper background grid. Efficient data structures have been implemented. The geometry is defined by a set of surface patches. The surface patch connectivity is computed by the grid generator. The surface triangle grid and volume tetrahedra grid are automatically generated. The grid cell sizes may be adapted to surface curvature.

5 Flow Solver

The flow solver EDGE [1], has been used for the flow computations. It solves the com-

pressible Euler / Reynolds Averaged Navier-Stokes (RANS) equations. The solver is a node-centered edge-based finite volume solver for arbitrary grid elements. The finite volume scheme is applied on the dual grid. The governing equations are integrated explicitly towards steady state with Runge-Kutta time integration. The convergence is accelerated with an agglomeration multigrid technique and implicit residual smoothing. Weak boundary conditions have been used for the computations in this paper. All solutions have been converged to residuals of about 10^{-12}.

6 Two-Dimensional Case: Inviscid Flow Around an Airfoil

Four different configurations have been studied: The 2D NACA 0012 configuration, Figures 1-2, the 2D double NACA 0012 configuration, Figures 3-4, the 2D double smooth TE configuration, Figure 5, and the 2D double smooth LTE configuration, Figure 6.

Grids have been generated for eight different grid resolutions, where the grids with grid spacing setting $h = 1.0$ are shown in Figures 1-6. The grids at other grid resolutions have been generated with uniformal coarsening/refinement by remeshing. The finest grids have around 500,000 nodes. For the NACA 0012 configuration computations have been done at $\alpha = 0.00°$, $\alpha = 1.25°$ and $\alpha = 2.50°$.

The results are summarized in Table 1-2. In Figure 8 and Table 4 for the NACA 0012 configuration at $\alpha = 0.00°$ it can be seen that there is a total pressure loss at the trailing edge, which is not decreasing with finer grid resolution, in contrast to the total pressure loss at the leading edge, which reduce with an approximate order of accuracy of 1.6, as expected.

The aim of this paper is to study the error at the trailing edge of a wing and see if this error influence the overall results. A sharp trailing edge introduce a jump in the slope of the geometry and there will be no well defined normal direction when implementing the boundary condition at this point. This jump is not reduced when reducing the grid cell sizes. Furthermore the error introduced here may be located at a very critical region of the geometry. Compare with two-dimensional theory for potential flow, where the circulation for the entire airfoil is decided by the introduction of the Kutta condition at the trailing edge.

It is well known that the type of finite volume flow solver used in this study gives a pressure peak at the trailing edge of an airfoil. Therefore three other configurations are also investigated in this study. In these configurations the airfoil is splitted into two parts and placed at the walls of the computational box, instead of in the middle. This was done in order to see if this reduce the error at the trailing edge. The double configurations with smooth leading and trailing edges have been studied in order to completely eliminate the jump in the slope at these points, and to see if this improves the convergence further.

In Figure 9 the typical pressure peak at the trailing edge can be seen for the NACA 0012 configuration, which is not present for the double NACA 0012 configuration. In Table 1 it can also be seen that the NACA 0012 configuration gives $C_L = 7.32 \cdot 10^{-4}$ compared to $C_L = -2.27 \cdot 10^{-7}$ for the double NACA 0012 configuration, for the finest grid resolution. This configuration clearly gives a much better result. The Pressure distributions for the double smooth TE and the double smooth LTE configurations are shown in Figure 10.

In Figures 11-12 the convergence order for C_D is plotted for the four studied configurations. It can be seen in Figure 11 that they all have a convergence order of about 2.0 for coarse grids, but it can also be seen in Figure 12 that the NACA 0012 configuration has a convergence order of 1.0 for very fine grids, in contrast to the double configurations still having a convergence order of around 2.0. Thus, the error at the trailing edge for the

NACA 0012 configuration clearly introduce an error in the overall C_D. The convergence of C_D for the NACA 0012 configuration is in accordance with the viscous results obtained in [3]. The error in C_D is 0.7 drag counts for a grid resolution $h = 0.5$.

The change in slope for the double smooth TE and the double smooth LTE configurations in Figures 11-12 for coarse grids is probably due to the fact that the pressure distributions for these configurations, se Figure 10, differs from the double NACA 0012 configuration. Thus the solution at the middle of the airfoil may not be resolved for the coarse grids. For fine resolution grids the convergence is slightly better than for the double NACA 0012 configuration.

In Figure 14 C_L is plotted for different grid resolutions. It can be seen that the error even for very fine grids is about 0.002. This does not seem to be reduced by finer grids.

Figure 15 shows the difference in C_p between the lower side and the upper side integrated along the chord. The value at $x = 1.0$ is thus equal to C_L. It can be seen, by the wiggles in the curves for the coarse grids, there are local errors along the chord, but for fine resolutions the curves are smooth. This clearly shows the non-symmetric solution. It can be seen that the contribution to the lift is about the same over the entire chord, but little larger at leading and trailing edges. Thus, the error in the pressure at the trailing edge introduce an erroneous circulation.

7 Three-Dimensional Case: Inviscid Flow Around a Wing Section

The studied configuration in 3D is the same as the 2D NACA 0012 configuration, but with a spanwise extension of 5.0 m. Six grids of different resolutions were generated. The grids have the same resolutions as the 2D NACA 0012 configuration, with the finest grid having around 7.5 Mpoints in total and around 250,000 surface points. In spanwise direction grid stretching is applied with a maximum stretching of 1:8 at the leading edge, see Figure 7. The results are summarized in Table 3, where also the results for the symmetric grids in 2D and 3D are given. In the symmetric grids each point on the upper side of the airfoil/wing surface have a corresponding point at the lower side.

The order of accuracy for C_D is shown in Figure 13. Here it can be seen that the order of accuracy is 2.0 for coarse grids and about 1.5 for fine grids. This is higher than for the corresponding 2D case, where it was 1.0. Figure 14 also shows that the error in C_L is much lower than for the 2D case.

Figure 16 shows the difference in C_p between the lower side and the upper side integrated along the chord for eight spanwise stations. It can be seen, by the wiggles, that the local error is higher than in Figure 15 for the 2D case at the corresponding grid resolution. How can the global error be smaller for the 3D case than for the 2D case if the local error is larger? A hint may be given by Figures 17-18 where the difference in C_p between the lower side and the upper side is given along the spanwise direction at four chordwise stations. Here it can be seen that the error in C_p is both positive and negative. So the errors may cancel out. This can more clearly be seen in Figure 19-20, where the difference in C_p is integrated in the spanwise direction. If comparing e.g. Figure 20 with Figure 18 it can be seen that the integrated value is only about 0.01 of a typical local value.

8 Conclusion

It has been shown that the local error introduced by the sharp trailing edge for an airfoil or a wing using a node-centered finite volume solver also gives rise to a small global error. The accuracy order of C_D drops to about 1.0 for very fine grids, and the error in C_L is about 0.002 even for very fine grids for low angles of attack for a simple airfoil in 2D. In 3D the errors are smaller. The accuracy order of C_D is about 1.5 and the error in C_L is

much smaller than in the corresponding 2D case, mostly due to error cancellation. The errors in these computations are very small but may be larger for e.g. compressible flow where the position of the shock is influenced by the error in the circulation.

References

[1] Eliasson, P., EDGE, a Navier-Stokes Solver for Unstructured Grids. Proceedings of Finite Volumes for Complex Applications III, ISBN 1-9039-9634-1, pp. 527-534, 2002.

[2] Eliasson, P. & Peng, S-H., Drag Prediction for the DLR-F6 Wing-Body Configuration Using the Edge Solver. Paper AIAA-2007-0897, 2007.

[3] Eliasson, P., Peng, S-H. & Tysell, L., Effect of Edge-based Discretization Schemes in Computations of the DLR F6 Wing-Body Configuration. Paper AIAA-2008-4153, 2008.

[4] Mavripilis, D., Grid Resolution Study of a Drag Prediction Workshop Configuration Using the NSU3D Unstructured Mesh Solver. Paper AIAA-2005-4729, 2005.

[5] Mavripilis, D., Vassberg, J., Tinoco, E., Mani, M., Brodersen, O., Eisfeld, B., Wahls, R., Morrison, J. Zickuhr, T. Levy, D. & Murayama, M., Grid Quality and Resolution Issues from the Drag Prediction Workshop Series. Paper AIAA-2008-0930, 2008.

[6] Svärd, M. Gong, J., & Nordström, J., An accuracy evaluation of unstructured node-centred finite volume. methods. *Applied Numerical Mathematics*, **58**(8), pp. 1142-1158, 2008,.

[7] Tysell, L., An Advancing Front Grid Generation System for 3D Unstructured Grids. ICAS Paper ICAS-94-2.5.1, pp. 1552-1564, Anaheim, California, USA, 1994.

[8] Tysell, L., Hybrid Grid Generation for Complex 3D Geometries. Proceedings of the *7th International Conference on Numerical Grid Generation in Computational Field Simulations*, pp. 337-346, International Society of Grid Generation (ISGG), Whistler, British Columbia, Canada, 2000.

[9] Tysell, L., The TRITET Grid Generation System. Proceedings of the *10th ISGG Conference on Numerical Grid Generation*, International Society of Grid Generation (ISGG), Forth, Crete, Greece, 2007.

[10] Tysell, L. and Nordström, J., Accuracy Evaluation of the Unstructured Node-Centered Finite Volume Method in Aerodynamic Computations. Proceedings of the *10th ISGG Conference on Numerical Grid Generation*, International Society of Grid Generation (ISGG), Forth, Crete, Greece, 2007.

[11] Vassberg, J., Tinoco, E., Mani, M., Brodersen, O., Eisfeld, B., Wahls, R., Morrison, J., Zickur, T., Laflin, K. & Mavripilis, D., Abridged Summary of the Third AIAA Computational Fluid Dynamics Drag Prediction Workshop. *AIAA Journal*, **45** (3), pp. 781-797, 2008.

Copyright Statement

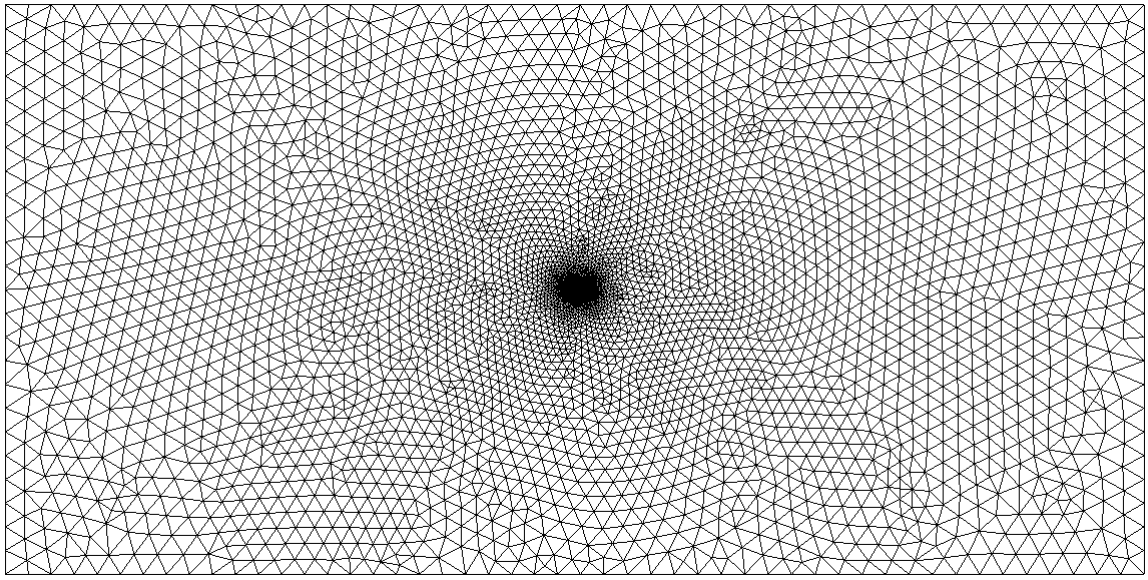

Fig. 1 Grid around the NACA 0012 airfoil. Grid resolution $h = 1.0$. Farfield view.

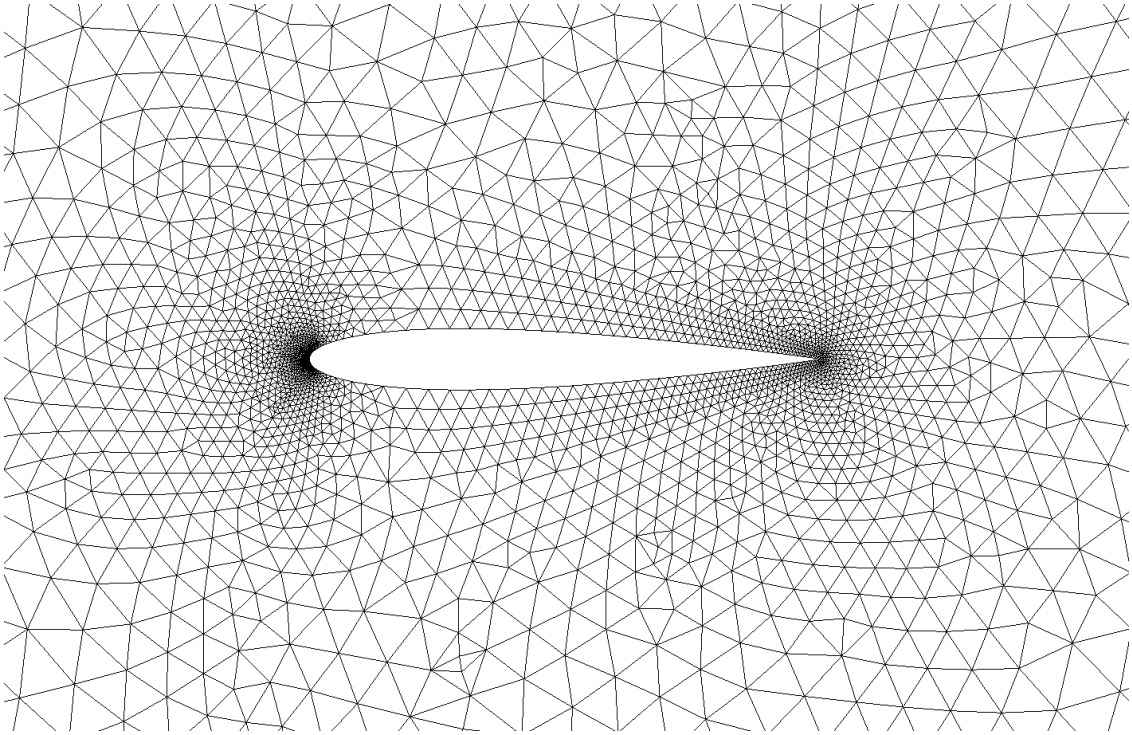

Fig. 2 Grid around the NACA 0012 airfoil. Grid resolution $h = 1.0$. Close-up view.

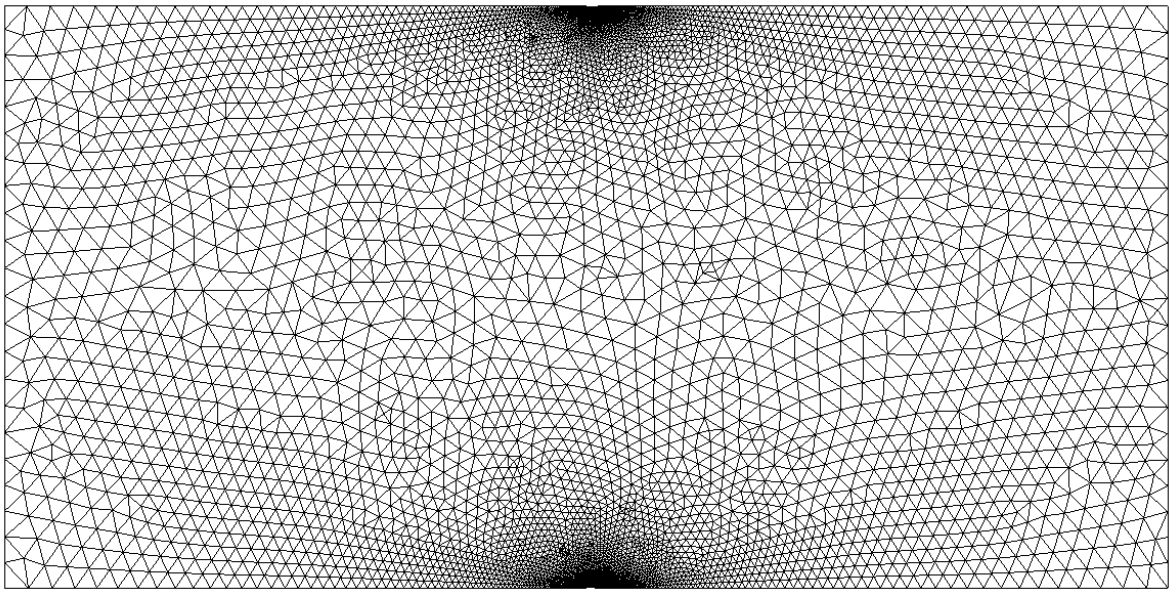

Fig. 3 Grid around the double NACA 0012 airfoil. Grid resolution $h = 1.0$. Farfield view.

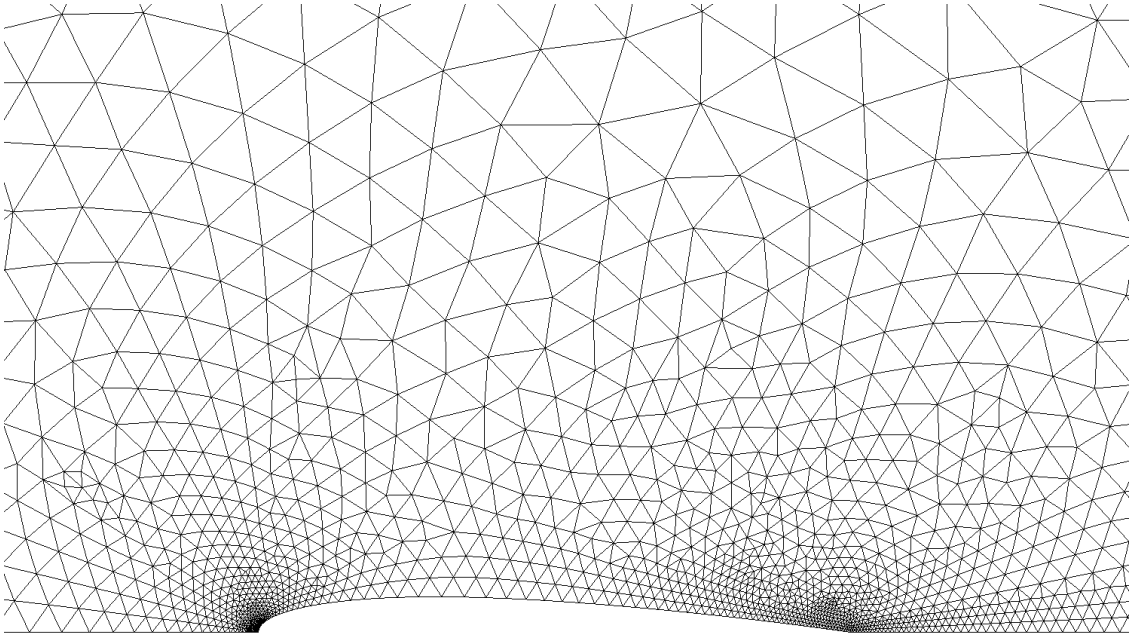

Fig. 4 Grid around the double NACA 0012 airfoil. Grid resolution $h = 1.0$. Close-up view.

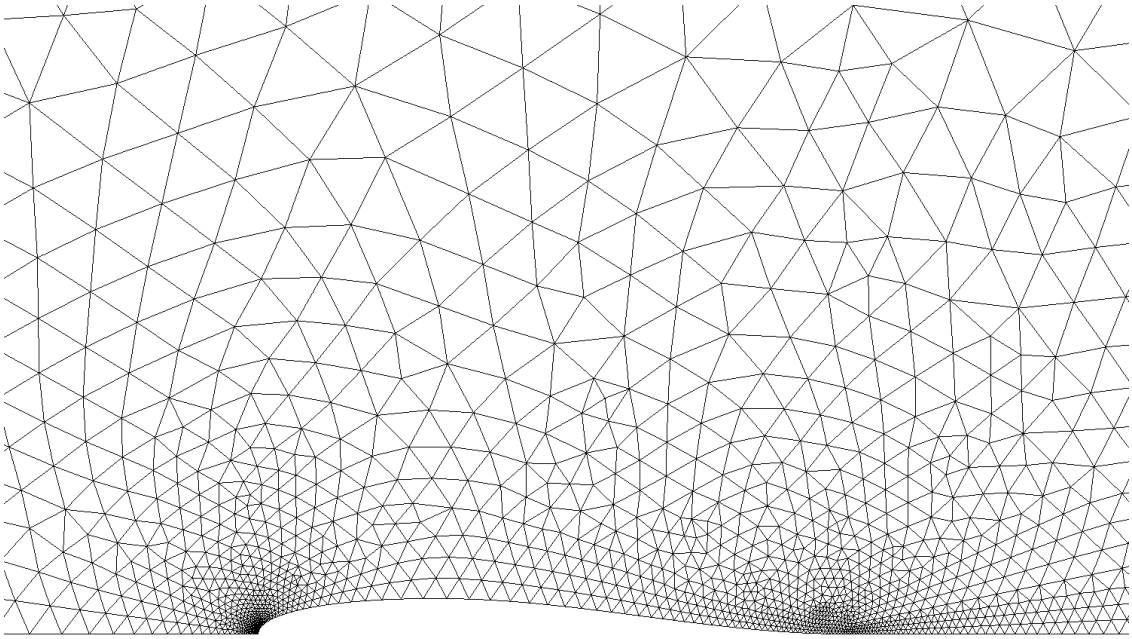

Fig. 5 Grid around the double smooth TE airfoil. Grid resolution $h = 1.0$. Close-up view.

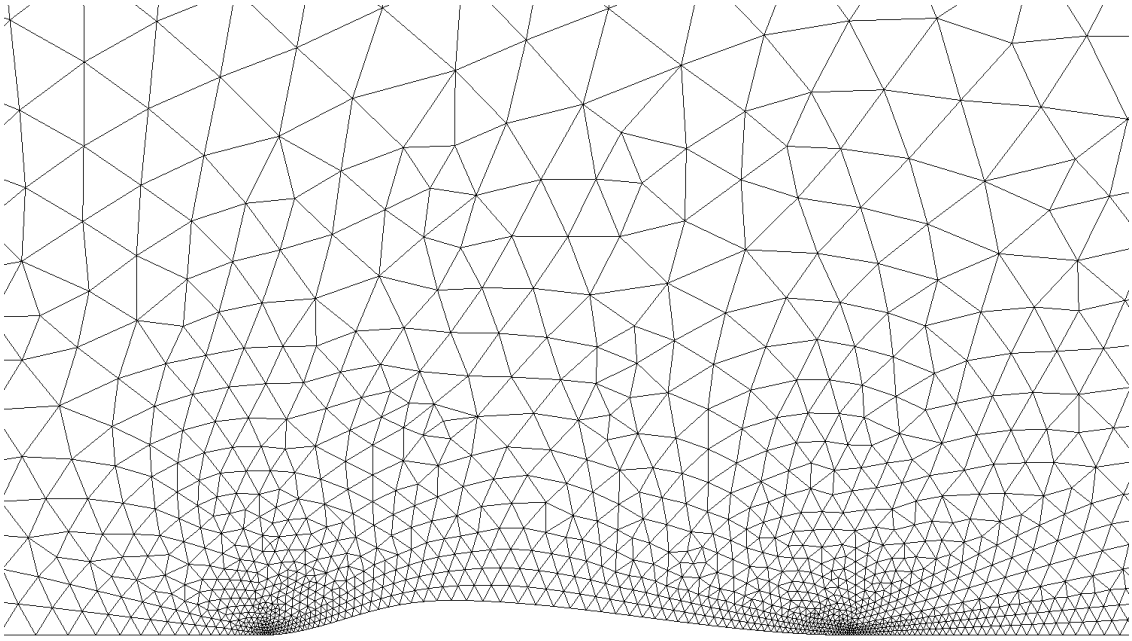

Fig. 6 Grid around the double smooth LTE airfoil. Grid resolution $h = 1.0$. Close-up view.

	NACA 0012		Double NACA 0012		Double smooth TE		Double smooth LTE	
h	C_L	C_D	C_L	C_D	C_L	C_D	C_L	C_D
16.0	-2.56E-2	2.35E-2	4.28E-3	2.96E-2	7.13E-3	1.51E-2	8.17E-3	1.63E-2
8.0	-4.89E-3	6.75E-3	-1.64E-3	8.37E-3	-5.09E-4	4.61E-3	2.48E-3	1.00E-2
4.0	-1.63E-3	1.72E-3	-6.12E-4	1.15E-3	-3.87E-4	6.28E-4	3.68E-4	2.61E-3
2.0	3.26E-3	5.00E-4	-2.92E-4	3.13E-4	-1.57E-4	1.60E-4	1.45E-4	4.87E-4
1.0	3.53E-3	1.56E-4	-1.15E-5	5.61E-5	-4.34E-5	4.74E-5	6.93E-6	7.59E-5
0.5	-3.09E-3	7.09E-5	6.88E-6	2.36E-5	-5.63E-6	1.89E-5	2.28E-6	1.50E-5
0.25	1.87E-3	3.40E-5	-1.00E-6	9.56E-6	-2.64E-6	6.71E-6	6.19E-7	5.26E-6
0.125	7.32E-4	1.56E-5	-2.27E-7	5.25E-6	-5.28E-7	3.72E-6	6.66E-8	2.42E-6

Table 1 C_L and C_D for the 2D configurations at zero angle of attack.

	NACA 0012 : $\alpha = 0.00°$		NACA 0012 : $\alpha = 1.25°$		NACA 0012 : $\alpha = 2.50°$	
h	C_L	C_D	C_L	C_D	C_L	C_D
16.0	-2.56E-2	2.35E-2	9.29025E-2	2.26E-2	2.68470E-1	2.21E-2
8.0	-4.89E-3	6.75E-3	1.55466E-1	6.43E-3	3.10335E-1	8.86E-3
4.0	-1.63E-3	1.72E-3	1.61023E-1	1.63E-3	3.14943E-1	1.95E-3
2.0	3.26E-3	5.00E-4	1.57736E-1	5.84E-4	3.13438E-1	5.38E-4
1.0	3.53E-3	1.56E-4	1.60785E-1	1.86E-4	3.16879E-1	1.94E-4
0.5	-3.09E-3	7.09E-5	1.57132E-1	7.33E-5	3.17526E-1	7.79E-5
0.25	1.87E-3	3.40E-5	1.57222E-1	3.38E-5	3.18298E-1	3.84E-5
0.125	7.32E-4	1.56E-5	1.60627E-1	1.72E-5	3.18569E-1	2.01E-5

Table 2 C_L and C_D for the 2D NACA 0012 configurations at different angles of attack.

	2D NACA 0012		2D NACA 0012 : sym		3D NACA 0012		3D NACA 0012 : sym	
h	C_L	C_D	C_L	C_D	C_L	C_D	C_L	C_D
16.0	-2.56E-2	2.35E-2	-4.29E-2	2.30E-2	2.31E-3	1.13E-2		
8.0	-4.89E-3	6.75E-3	-1.41E-2	6.85E-3	1.90E-3	2.93E-3		
4.0	-1.63E-3	1.72E-3	7.35E-4	1.82E-3	1.23E-3	1.03E-3		
2.0	3.26E-3	5.00E-4	-1.69E-3	5.04E-4	-2.20E-5	4.16E-4	3.40E-4	4.18E-4
1.0	3.53E-3	1.56E-4	-4.50E-4	1.87E-4	-4.01E-4	1.82E-4	2.15E-4	2.05E-4
0.5	-3.09E-3	7.09E-5	1.46E-4	6.23E-5	1.19E-4	8.59E-5		
0.25	1.87E-3	3.40E-5	-2.68E-4	3.76E-5				
0.125	7.32E-4	1.56E-5	-4.57E-4	1.51E-5				

Table 3 C_L and C_D for the 2D and 3D NACA 0012 configuration at zero angle of attack. The symmetric grids have symmetric surface grids only.

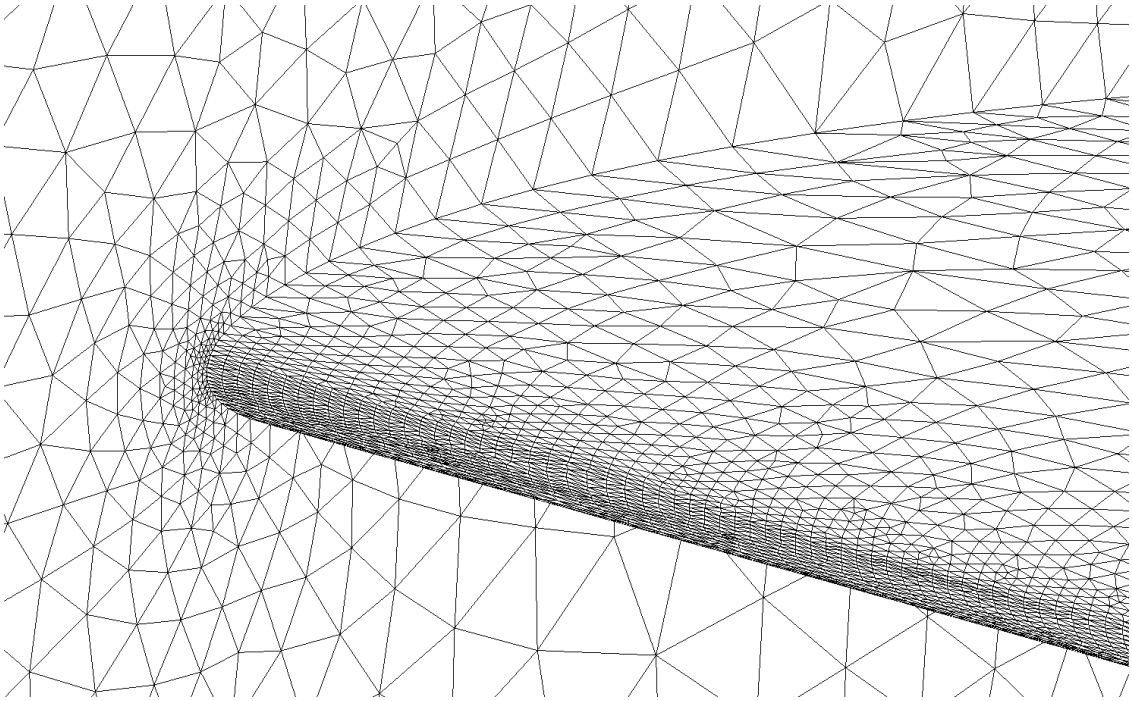

Fig. 7 Grid around the 3D NACA 0012 wing at wing leading edge and symmetry plane. Grid resolution $h = 2.0$. Close-up view.

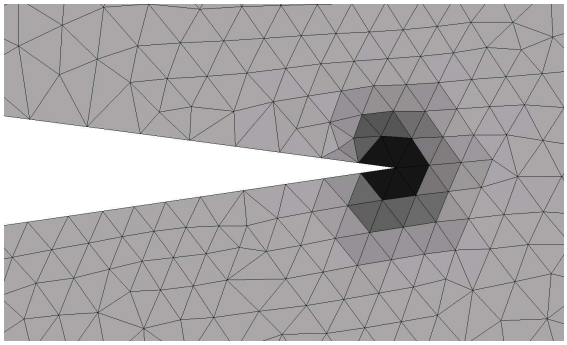

Fig. 8 Change in total pressure within one cell at trailing edge for the 2D NACA 0012 configutation at $\alpha = 0.0°$.

h	ΔP_{tot} LE %	ΔP_{tot} % TE
16.0	3.36	0.709
8.0	1.80	1.045
4.0	8.58E-01	0.939
2.0	3.40E-01	1.042
1.0	4.02E-02	1.063
0.5	5.54E-03	0.959
0.25	1.55E-03	0.990
0.125	6.65E-04	0.886

Table 4 Change in total pressure within one cell at leading and trailing edge for the 2D NACA 0012 configuration at $\alpha = 0.0°$.

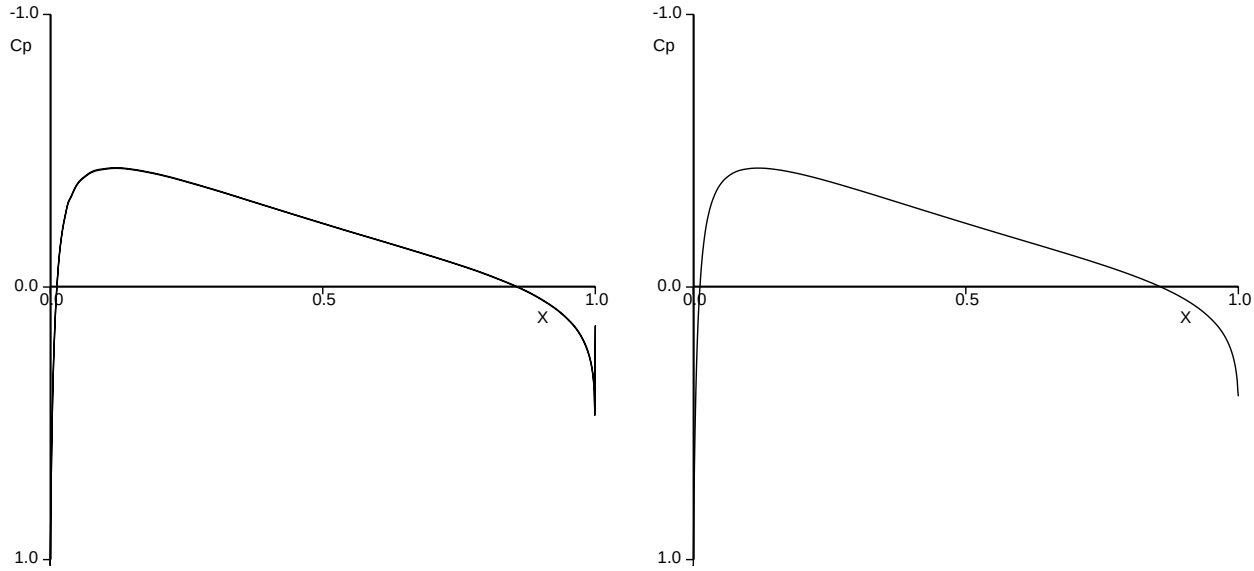

Fig. 9 $C_p(x)$ for the 2D NACA 0012 configuration (left) and the 2D double NACA 0012 configuration (right) for grid resolution $h = 0.25$.

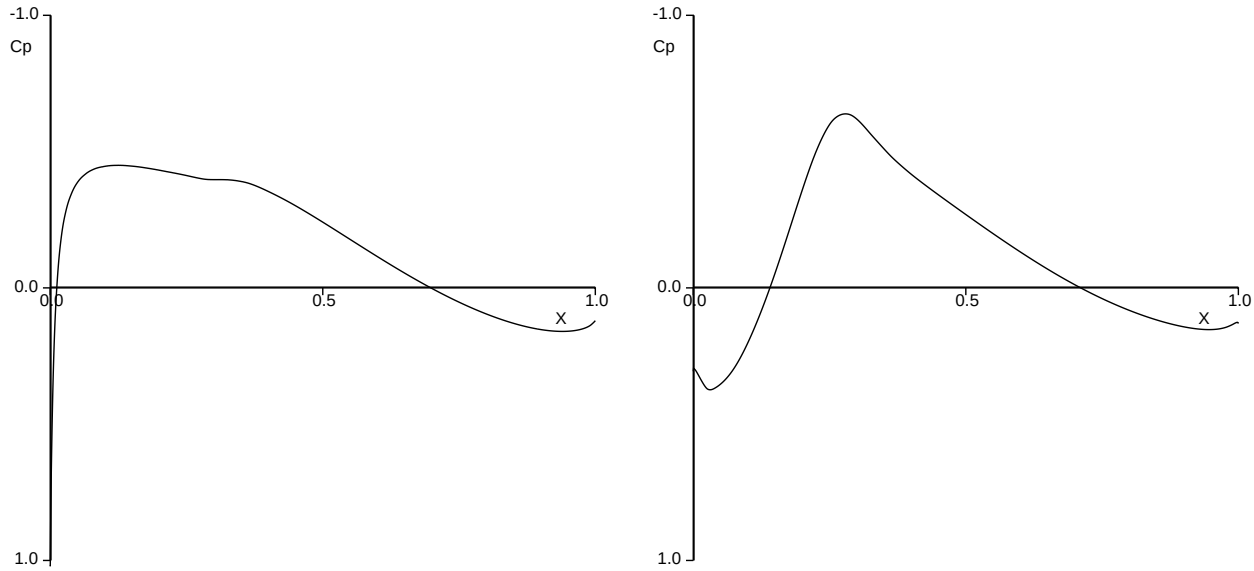

Fig. 10 $C_p(x)$ for the 2D double smooth TE configuration (left) and the 2D double smooth LTE configuration (right) for grid resolution $h = 0.125$.

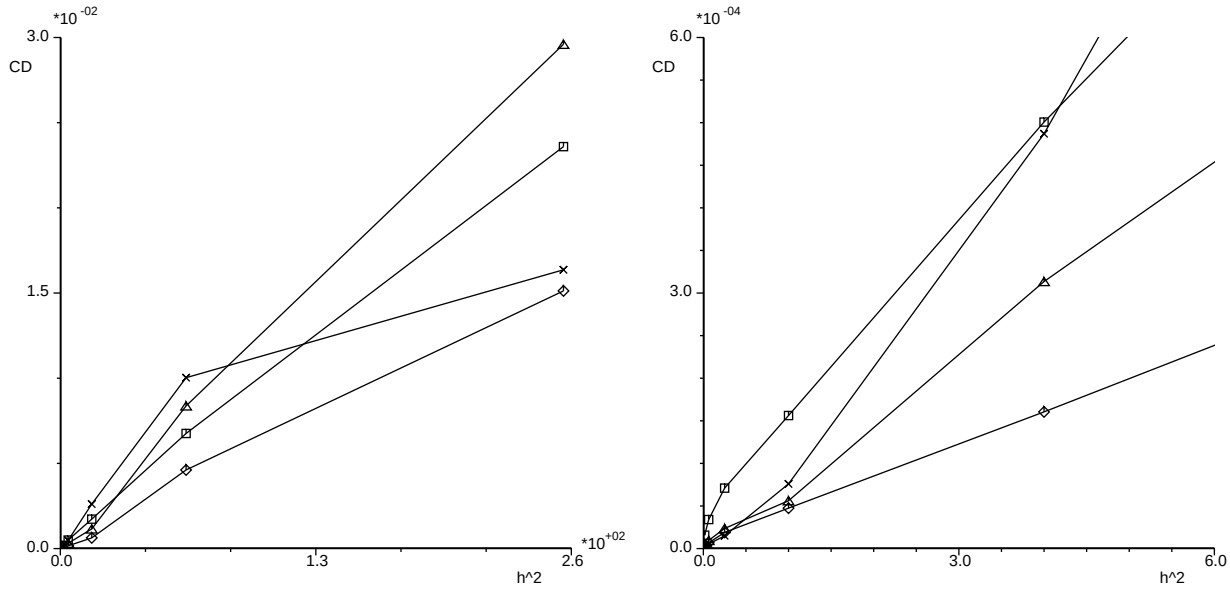

Fig. 11 C_D vs. h^2 for the 2D configurations. ⊡ → NACA 0012. △ → Double NACA 0012. ⋄ → Double smooth TE. × → Double smooth LTE.

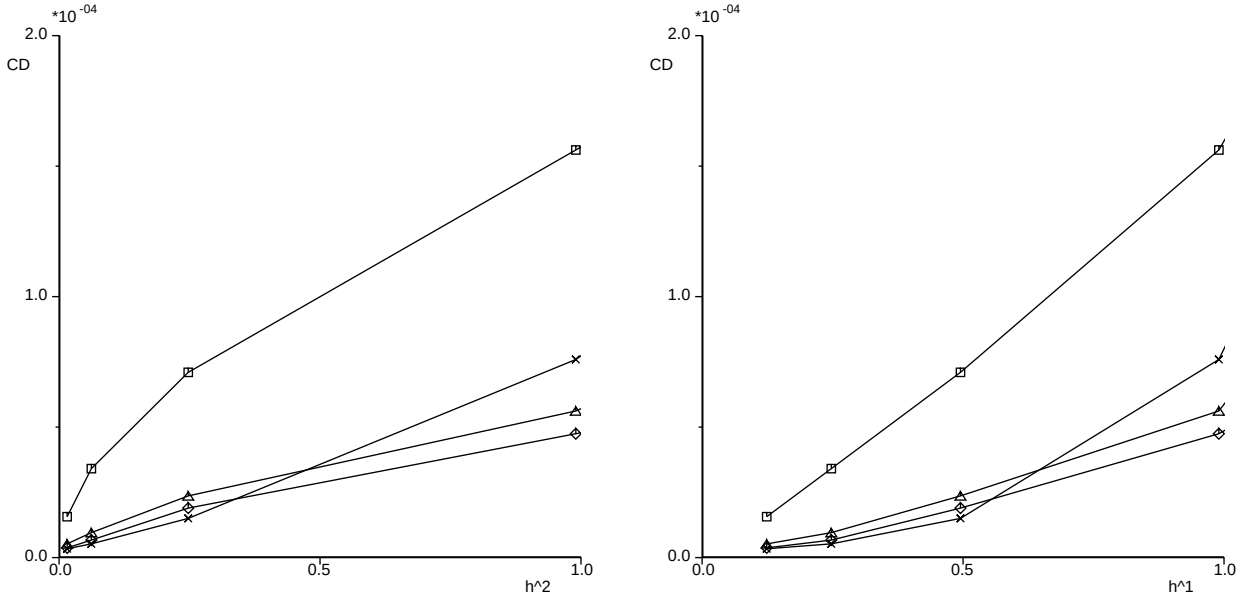

Fig. 12 C_D vs. h^2 (left) and h^1 (right) for the 2D configurations. ⊡ → NACA 0012. △ → Double NACA 0012. ⋄ → Double smooth TE. × → Double smooth LTE.

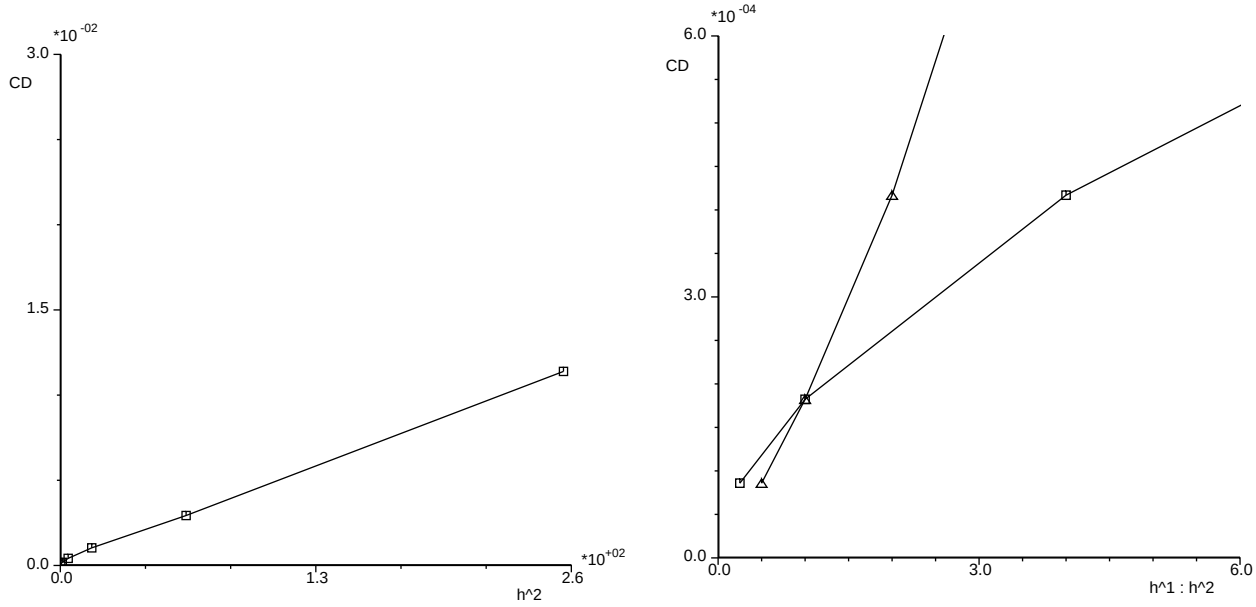

Fig. 13 C_D vs. h^2 (left) and h^1 (△) & h^2 (⊡) (right) for the 3D NACA 0012 configuration.

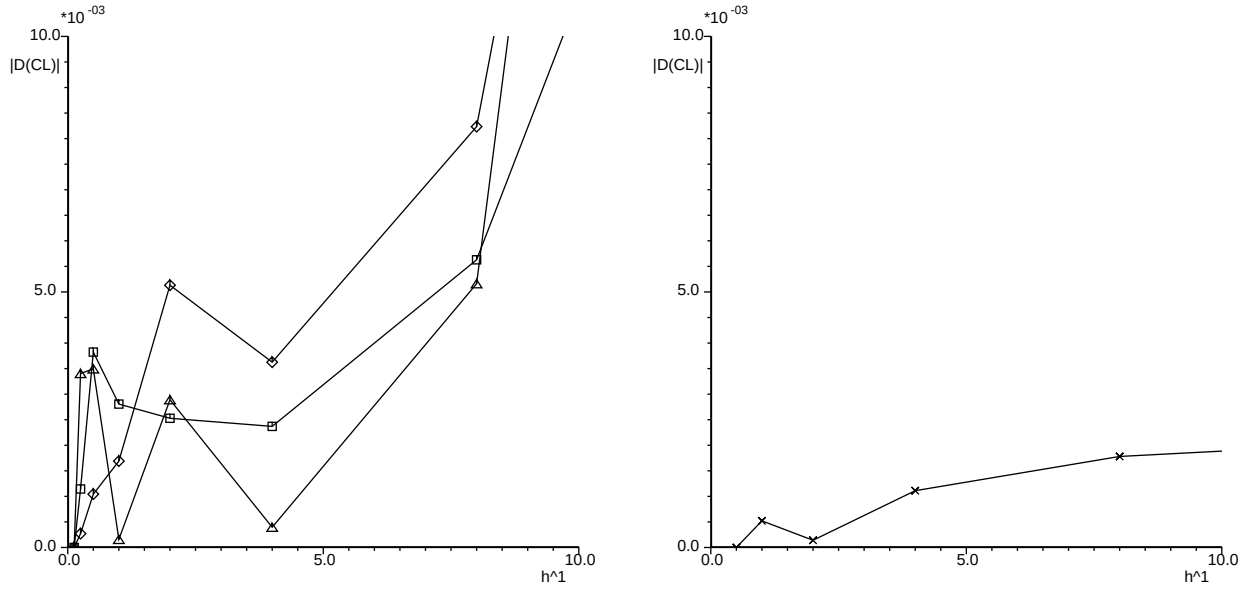

Fig. 14 $|C_L - C_L(finest\ grid)|$ for the 2D (left) and 3D (right) NACA 0012 configurations, ⊡ → 2D: $\alpha = 0.0°$. △ → 2D: $\alpha = 1.25°$. ◇ → 2D: $\alpha = 2.50°$. × → 3D: $\alpha = 0.0°$.

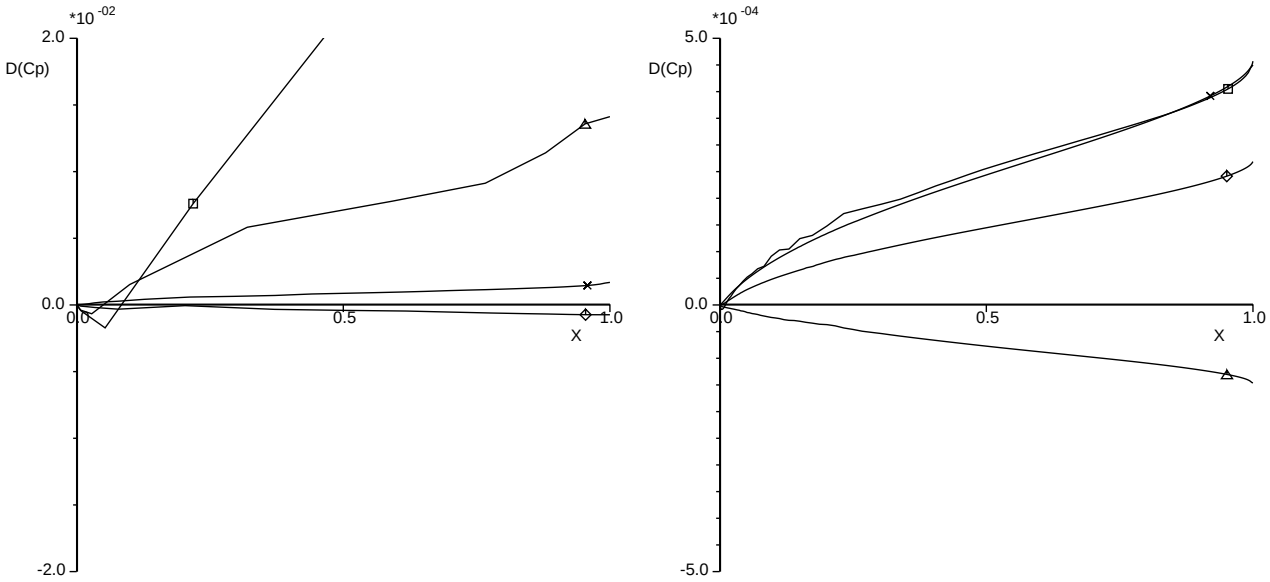

Fig. 15 $\int_0^x C_p(x)(lower - upper)dx$ for the 2D NACA 0012 configuration, with symmetric surface node distribution. $\boxdot \rightarrow h = 16.0$ (left) and 1.0 (right). $\triangle \rightarrow h = 8.0$ and 0.5. $\diamond \rightarrow h = 4.0$ and 0.25. $\times \rightarrow h = 2.0$ and 0.125.

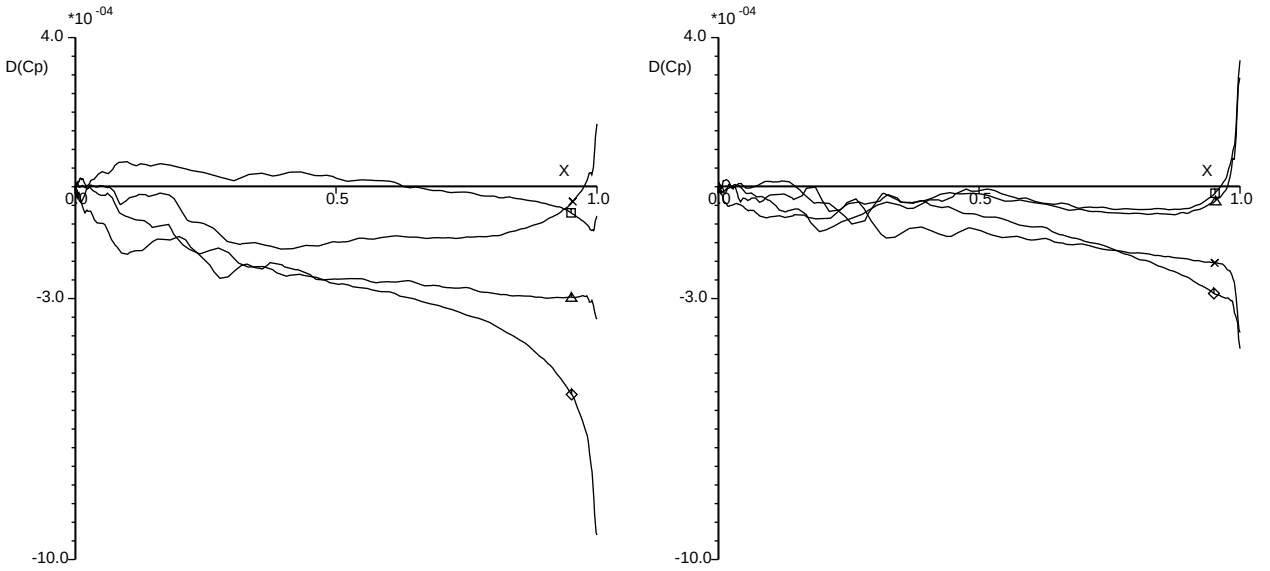

Fig. 16 $\int_0^x C_p(x)(lower - upper)dx$ for the 3D NACA 0012 configuration, with symmetric surface node distribution for grid resolution $h = 1.0$. $\boxdot \rightarrow$ z-station = 0.1 (left) and 0.5 (right). $\triangle \rightarrow$ z-station = 0.2 and 0.6. $\diamond \rightarrow$ z-station = 0.3 and 0.7. $\times \rightarrow$ z-station = 0.4 and 0.8.

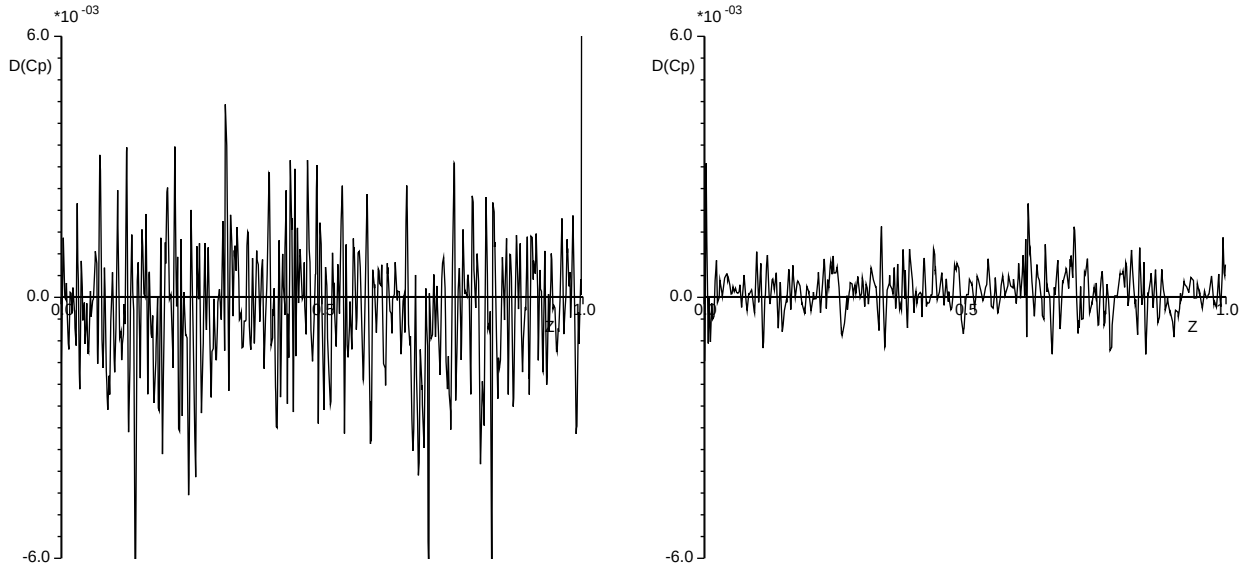

Fig. 17 $C_p(z)(lower - upper)$ along spanwise direction z for the 3D NACA 0012 configuration, with symmetric surface node distribution for grid resolution $h = 1.0$ at $x-$station$= 0.1$ (left) and $x-$station$= 0.5$ (right).

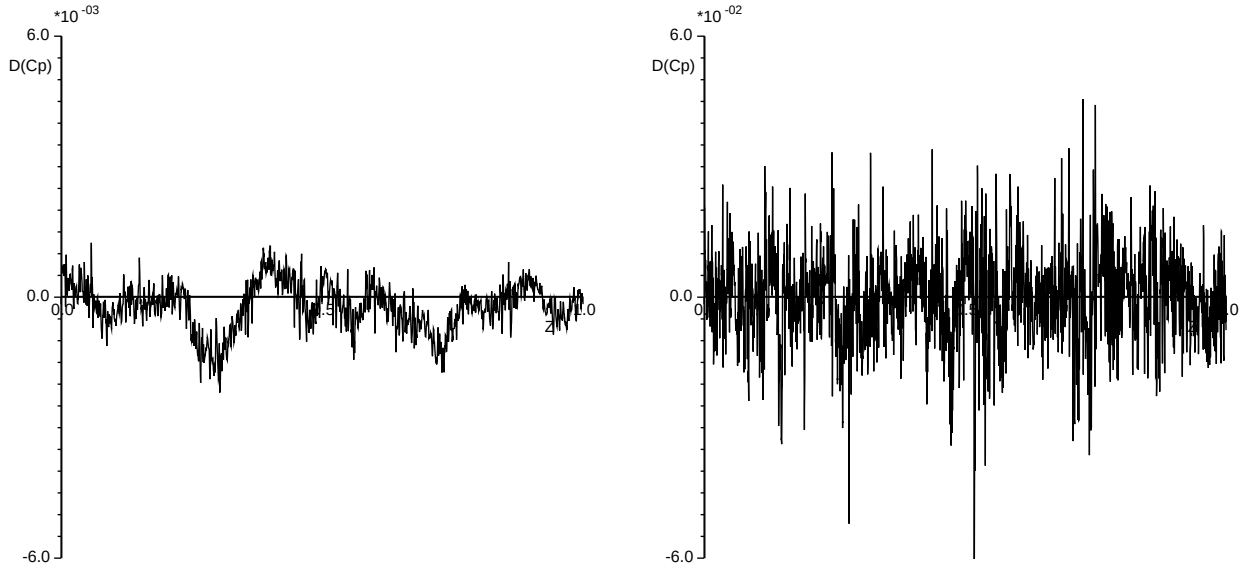

Fig. 18 $C_p(z)(lower - upper)$ along spanwise direction z for the 3D NACA 0012 configuration, with symmetric surface node distribution for grid resolution $h = 1.0$ at $x-$station$= 0.9$ (left) and $x-$station$= 0.99$ (right).

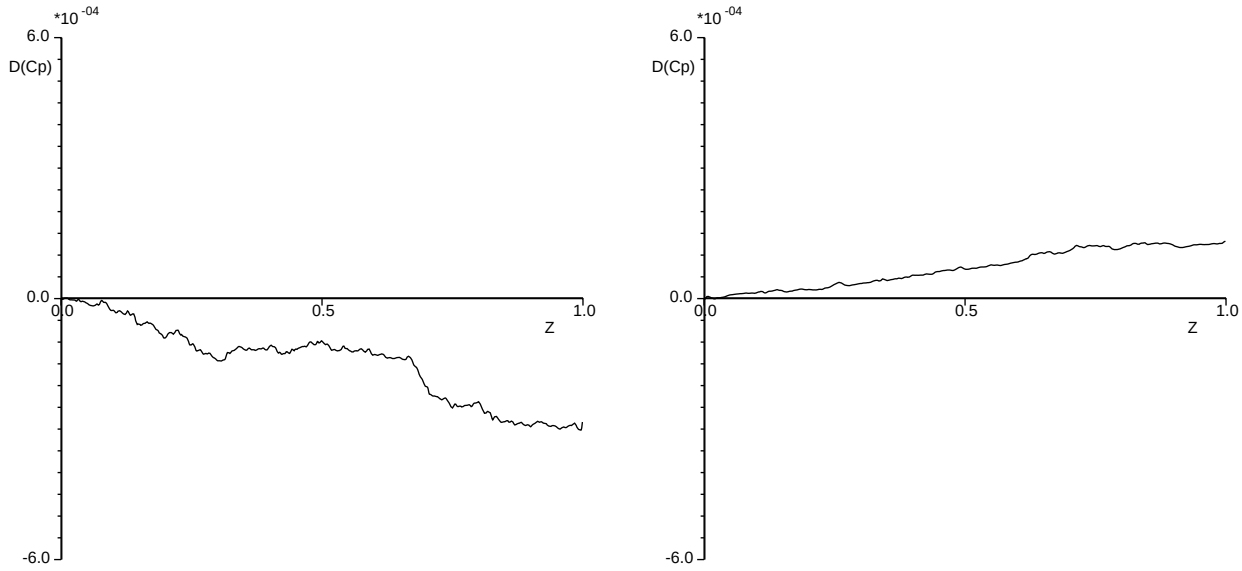

Fig. 19 $\int_0^z C_p(z)(lower - upper)dz$ for the 3D NACA 0012 configuration, with symmetric surface node distribution for grid resolution $h = 1.0$ at $x-$station$= 0.1$ (left) and $x-$station$= 0.5$ (right).

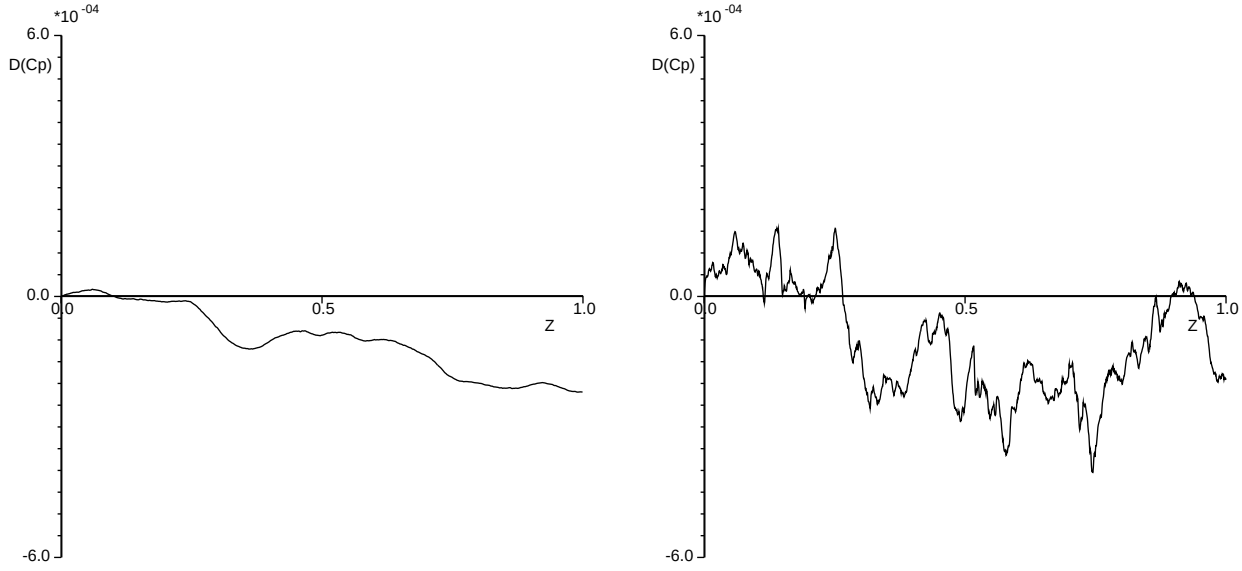

Fig. 20 $\int_0^z C_p(z)(lower - upper)dz$ for the 3D NACA 0012 configuration, with symmetric surface node distribution for grid resolution $h = 1.0$ at $x-$station$= 0.9$ (left) and $x-$station$= 0.99$ (right).